A Compact Gas Liquid Separator for the SNS Mercury Process Loop

Charlotte Barbier[1]
Oak Ridge National Laboratory, Oak Ridge, TN
barbiercn@ornl.gov
ASME Membership: 000100132392

Elvis Dominguez-Ontiveros
Oak Ridge National Laboratory, Oak Ridge, TN
dominguezoee@ornl.gov

Justin Weinmeister
Oak Ridge National Laboratory, Oak Ridge, TN
weinmeistejr@ornl.gov
ASME Membership: 000103307425

Jeremy Slade
Oak Ridge National Laboratory, Oak Ridge, TN
sladejp@ornl.gov

Dustin Ottinger
Oak Ridge National Laboratory, Oak Ridge, TN
ottingerdd@ornl.gov

Robert Sangrey
Oak Ridge National Laboratory, Oak Ridge, TN
sangreyrl@ornl.gov

[1] Corresponding author information can be added as a footnote.

ABSTRACT

Upgrades at the Spallation Neutron Source (SNS) accelerator at Oak Ridge National Laboratory are underway to double its proton beam power from 1.4 to 2.8 MW. About 2MW will go to the current first station while the rest will go to the future Second Target Station. The increase of beam power to the first target station is especially challenging for its mercury target. When the short proton beam hits the target, strong pressure waves are generated, causing cavitation erosion and challenging stresses for the target's weld regions. SNS has successfully operated reliably at 1.4 MW by mitigating the pressure wave with the injection of small Helium bubbles into the mercury. To operate reliably at 2MW, more gas will be injected into mercury to mitigate the pressure wave further. However, the mercury process loop was not originally designed for gas injection, and the accumulation of gas in the pipes is a concern. Due to space constraints, a custom Gas Liquid Separator (GLS) was designed to fit a 90-degree horizontal elbow space in the SNS mercury loop. Simulations and experiments were performed, and a successful design was developed that has the desired efficiency while keeping the pressure losses acceptable.

INTRODUCTION

The Spallation Neutron Source (SNS) at Oak Ridge National Laboratory (ORNL) generates neutrons by bombarding a heavy metal target with a powerful 1.4 MW 60 Hz pulsed proton beam. At SNS, the liquid mercury target is contained within a stainless steel vessel which connects to the process piping. More details on the flow pattern inside the target can be found in [1]. When the beam hits the target, about 65% of the energy is deposited as heat into the mercury in less than a microsecond. The isochoric heat deposition leads to strong pressure waves that propagate in both the mercury and stainless steel. These pressure waves cause the mercury to cavitate, and erosion damages have been observed [2]. To date, the target has leaked because of fatigue failure at the

welds or cavitation erosion of the vessel wall. Early in the development of the SNS target, it was suggested to inject small bubbles into the mercury to mitigate the pressure wave; an extensive summary of the research can be found in [3]. However, such a system was not originally implemented at SNS, but after several target failures, a gas injection system was eventually implemented in late 2017 [4]. Despite the small quantity of helium gas injected (0.4 SLPM), or about 0.02% of the mercury flow rate (250 GPM or 950 LPM), significant stress reduction was observed [5]. As of early 2021, 8 targets have been operated with a gas injection rate ranging from 0.2 to 3.5 SLPM. Post-irradiation examination suggests that further mitigation is achieved at higher gas injection rates.

Upgrades at SNS are currently underway to increase the proton beam power from 1.4 MW to 2.8 MW. About 2 MW will go to the current mercury target while the rest will go to the future rotating target of the Second Target Station. Since the pressure wave strength is proportional to the beam power, additional mitigation will be required by injecting more gas (up to 20 SLPM) into the target. One major concern is the accumulation of gas in the mercury process loop, which could lead to increased pressure losses, eventually causing the pump to stall. The SNS mercury process loop is shown in Figure 1: the flow is discharged at 250 GPM, and then split into three branches to feed the three target inlets. The flow combines in the target, is heated by the proton beam, and then exits the target. The mercury then flows towards the heat exchanger before going back to the pump. Gas accumulation in the process loop can be measured by monitoring the mercury level in the pump tank: the amount of mercury rise in the pump tank is equivalent to the volume of gas accumulated in the loop. To date, the gas volume

accumulating in the loop is linear with the gas injection in the target (see Figure 2). If it keeps following the linear trend, about 70 liters of gas will accumulate at 20 SLPM of He gas injection. This gas accumulation is an operational concern since it will reduce the headspace available in the pump tank, and in the case of a pump trip, the accumulated gas will expand towards the target, causing the pump to overflow. To address this risk, an overflow tank and a Gas-Liquid Separator (GLS) will be installed in the process loop. Since the mercury is highly activated from the proton beam, the process loop is located within a hot cell and is shielded with stainless steel blocks to limit radiation damage to the equipment in the cell. Additionally, all the upgrades must be done remotely with servo manipulators. Because of this, the only possible location for the GLS is at a horizontal 90-degree elbow between two Reflange connectors (Figure 1 and Figure 3). The GLS height is constrained by the floor below and the shielding above. No off-the-shelf GLS could fit the spatial constraint, so a custom GLS had to be developed. Non-geometric requirements for the GLS were an efficiency above 90% at the nominal flow rate (250 GPM) and a pressure loss factor less than 20.

Compact Gas-Liquid Separator

Separation of multiphase flows is frequently encountered in various fields including nuclear, chemical, oil & gas, food, waste processing, aerospace, and manufacturing. Proper design for a gas-liquid separator is important because a separator is usually an initial process component in a facility, and improper design may affect the performance of the entire system. The separation of the two fluids may be achieved through various methods such as gravity decantation, centrifugal forces, precipitation, or magnetic and

electrical field methods such as induced decantation and precipitation. Gravity separation is the most common method found in gas-liquid day-to-day applications. However, conventional gravity-based vessel type separators (or gravity settlers) are typically expensive and have a large footprint. Two types of gravity settlers exist, the vertically oriented and the horizontal oriented vessel [6]. Horizontal vessels are often used when the vessel must handle large amount of liquids, e.g. inlet separators on platforms. The vertical vessels are used when the fluid has a large gas to liquid ratio. While horizontal vessels often are called separators, vertical vessels handling large gas to liquid ratios are often called gas scrubbers [6].

Compared with vessel-type separators, compact separators such as the gas-liquid cylindrical cyclone (GLCC), are simple, low-cost, low-weight separators that require little maintenance and are easy to install and operate. The GLCC [6] consists of a vertical pipe with a tangentially inclined inlet and outlets for gas and liquid. The tangential flow from the inlet to the body of the GLCC creates a swirl that produces centrifugal force on the fluids that are an order of magnitude higher than the force of gravity. The combination of gravitational, centrifugal, and buoyancy forces separates the gas and liquid. The liquid is pushed radially outward and downward toward the liquid exit, while the gas is driven inward and upward toward the gas outlet. The compact GLCC separator offers an attractive alternative to the conventional vessel-type separator. These types of separators have been studied previously [6] and usually require a long cylindrical core with typical length to diameter ratios greater than 10 for maximum performance.

As mentioned earlier, the SNS Gas Liquid Separator (GLS) needed to fit in a tight place, be passive, reliable with low maintenance requirements, have acceptable pressure loss, capable of installation with servo-manipulator, have relatively large mass flow rates processing capacity, and radiation-resistant. Due to the spatial constraint, the vortex type separator design is the only option for the SNS. However, the typical configurations found in the literature and several commercially available designs failed to fulfill all the requirements. The large length to diameter ratio needed to achieve maximum performance in GLCCs was a limitation for this application. Therefore, a new separator design based on a hydro cyclone using vortex generation for gas-liquid separation was conceived to separate the activated liquid mercury and the helium gas-phase at SNS.

The new design consists of a cylindrical enclosure with a tangential inlet and outlet horizontally perpendicular to each other. This inlet-outlet arrangement allows the GLS to be installed in place of a regular 90-degree elbow using standard flanges or fittings as shown in Figure 4. A secondary structure with a conic shape is placed inside the cylindrical enclosure to promote rotational flow. The conic shape has feet that elevate the cone above the bottom of the enclosure. Thus, the liquid enters the enclosure and swirls around the cone before entering the bottom of the cone to be redirected towards the outlet (see Figure 4). The gas outlet is located at the top of the enclosure (Figure 4).

COMPUTATIONAL SETUP

A computational study was run of the proposed GLS to refine the prototype design and estimate its performance prior to testing. The model geometry was simplified prior to analysis by removing small features to ease meshing. The resulting model dimensions

can be seen in Figure 5 and the geometry with the boundaries in Figure 6. For the fluid domain, the inlet and outlet are about 150 mm in diameter, the cylinder housing is about 370 mm high and 400 mm in diameter with a 290 mm tall and 300 mm wide cone with a 24° pitch inside. The cone inlet is 150 mm in diameter and has a 16 mm gap between it and the bottom of the housing. The inlet and outlet were extended 1 m to ease convergence while the ventline was extended 2 m for two-phase simulations and closed for the single-phase simulations.

Simulations were meshed and run in ANSYS Fluent 2019 R2. Each case's mesh was a polyhedral-hexcore mesh with a minimum size of 0.5 mm and a maximum size of 8 mm with 10 inflation layers with a first cell height of 0.2 mm and a last aspect ratio of 0.272. This inflation layer setting targeted wall modeling of the turbulence, though the different regions of the GLS experienced large differences in near-wall velocities. The gas inlet face was meshed with 0.2 mm cell face sizes and had a body of influence refinement region 40 mm around the inlet with a maximum cell size of 2 mm. Mesh refinement was used as needed in regions with small gaps. A cross-section view of the mesh with a closed vent for single-phase simulations is shown in Figure 7.

The simulations were run with a coupled pressure-based solver in a pseudo-transient mode. Turbulence was modeled with the realizable k-epsilon Reynolds-Average Navier-Stokes (RANS) model with scalable wall functions. For two-phase simulations, the two-phase mixture used an Eulerian-Eulerian formulation with symmetric dragmodel and a drag coefficient of 0.44. The k-epsilon mixture model was utilized for turbulence. For the gas phase, the bubble size was fixed at 1 mm. Gravity forces were also included with

an operating density of 0.1625 kg/m^3. Each case was run for 5000 iterations, though the simulations were restarted from a prior momentum solution.

The boundary conditions were a specified mass flow rate of 200 kg/s (equivalent to 234 GPM) of mercury at the inlet, a pressure outlet at the vent line with 0 Pa specified, and a pressure outlet in the outlet line with 54,471 Pa specified. For two-phase simulations, the gas flow rate was 5.9533e-5 kg/s which is equal to the maximum expected maximum gas flow rate of 20 SLPM.

The particular two-phase formulation used in this simulation is not very accurate as it sacrifices many important physics in order to achieve stable solutions. Importantly, this model discounts the various flow regimes, , bubble coalescence and breakup behavior, and additional bubble forces other than drag. Discounting the various flow regimes and bubble coalescence and breakup affects the accuracy of the simulation since the flow enters the GLS as a stratified flow but converts to a bubbly flow within. However, no multi-regime model had been implemented in Fluent at the time of the work. The two-phase mixture approach was chosen over interface tracking methods because the behavior of small bubbles within the GLS was of most interest, and the accuracy lost in the inlet region would be inconsequential. Regardless, the GLS works best with large helium bubbles that have a large buoyant force but departure significantly from spherical and so are subject to shear breakup. Tracking this level of shear breakup was important for the design. As a proxy measurement, the turbulent forces in the GLS were compared for various designs to determine if geometry modifications induced significantly more shear forces on the helium bubbles.

A variety of computational studies were conducted to determine key design parameters of the GLS including a direct flow cone, the height of the GLS, removal of bottom space, and the introduction of several flow direction plates designed to increase efficiency. Additionally, two simulations were run with a Reynolds stress turbulence model to determine if the realizable k-epsilon turbulence model was missing major swirling-induced turbulence.

The simulations showed acceptable convergence for single-phase flow with the mass residual below 1e-3 and the momentum residuals all below 1e-5 (Figure 8). For the two-phase simulations, the residuals did not show steady convergence behavior due to unsteadiness in the gas phase, which created numerical instability in the entire solution (Figure 9). However, these simulations revealed the flow structures changed little, so the simulations were deemed sufficient for the current study.

A convergence study was also run to determine the mesh dependence of the solution. A coarse mesh with 0.5x refinement and a fine mesh with 2x refinement were both run and results are shown in Table 1. The first layer height of the inflation layers was not changed as it would greatly change the ratio of resolved to modeled boundary layer cells in the solution. The area of most concern was maintaining high quality cells for wall modeled turbulence in the housing interior and cone exterior, where the average first cell Y+ was 33 (in the low log-law region). As the area of interest was in the inlet and main body, errors in boundary layer resolution underneath the cone, near the vent, and in the recirculation region behind the outlet pipe were not aggressively eliminated. Results showed a variance of 0.6% for the vent pressure (1 in above the cone top) and 0.5% for

the cone inlet. This low discretization error gave confidence in the simulations' prediction of pressure loss for the geometries.

EXPERIMENTAL SETUP

A prototypical GLS with two cone inserts was built and tested at the Target Test Facility (TTF) at ORNL. The TTF was designed as a full-scale model of the SNS mercury process loop, except it does not have a large heat exchanger. To test the GLS, the TTF was modified to recreate the same piping section as the SNS loop at the GLS installation location. In particular, the following combination of 6-inch piping is repeated like in the SNS mercury process loop: a 2.1 m straight horizontal section, a horizontal 90-degree elbow, a 1 m straight horizontal section, a horizontal 90-degree elbow (or GLS test section), and a 0.6 m straight downward section as shown in Figure 10. Note that the "horizontal" sections have a 1-deg downward slope like at the SNS to allow proper draining of the loop.

Keeping the piping configuration as close as possible to the SNS process loop is important to make sure the multiphase flow regime is the same. With a mercury flow rate of 250 GPM (15.8 L/s) and a Helium gas injection rate of 10 SLPM, the mass velocities of the liquid G_l and gas G_g are respectively 11,463 kg/m^2/s and 1.60x10^{-3} kg/m^2/s. The flow regime was determined using the Baker's map [7], and the gas-phase parameter λ and the liquid-phase parameter ψ are calculated as follows:

$$\lambda = \left(\frac{\rho_g}{\rho_{air}}\frac{\rho_l}{\rho_{water}}\right)^{1/2}$$

$$\psi = \left(\frac{\sigma_{water}}{\sigma_l}\right)\left(\left(\frac{\mu_l}{\mu_{water}}\right)\left(\frac{\rho_{water}}{\rho_l}\right)^2\right)^{1/3}$$

Where $\rho_g, \rho_l, \rho_{air}$ and ρ_{water} are the densities of helium, mercury, air, and water respectively; μ_l and μ_{water} are the dynamic viscosities of mercury and water; and σ_l and σ_{water} are the surface tensions of mercury and water. The properties of air, water, and mercury are taken at standard atmospheric pressure and room temperature, whereas the helium is estimated at 6 psig, the pressure at the GLS inlet for a 250 GPM mercury flow rate. It is found that $G_l\psi \approx 350$ and $G_g/\lambda \approx 0.0001$, which corresponds to a stratified flow regime according to the Baker flow pattern map.

The flow regime was indeed confirmed to be stratified based on the observations made on the viewports upstream of the GLS test section (see Figure 10). To reach a faster steady state, gas was injected upstream of the first viewport: helium would accumulate only in the pipe section from the injection port to the GLS. At 250 GPM, a steady state is reached in less than an hour and is confirmed by a constant mercury level in the sump tank, which means that no more gas is accumulating in the piping. A mass flow controller is used to inject gas upstream of the GLS (Parker Porter LB-521) and a low DP mass flowmeter (Bronkhorst F-102E series) is used at the ventline to measure the GLS efficiency.

Figure 11 shows a 3D cross-sectional view of the prototypical GLS: the gas-liquid flow enters through the inlet and swirls around the cone. Due to centrifugal force and buoyancy, gas flows towards the ventline while the liquid is sucked at the base of the cone and then redirected towards the outlet. The lid is made of acrylic to observe the gas-liquid separation process, and a viewport was added on the GLS body to not only observe

potential bubbles but also to estimate the amount of mercury left in the GLS after draining the loop. The cone insert can be swapped once mercury is drained from the bottom of the GLS using the bottom drain port.

Just above the ventline, a Mott POU-10-S GasShield filter was installed (see Figure 12) to stop any mercury slugs entrained with the helium and protect the mass flowmeter. This filter has been extensively tested at the TTF and has demonstrated to be very efficient at blocking mercury while letting flowing helium as long as the differential pressure remained below ~25 psid: at higher differential pressures, the mercury will flow through the filter.

Two cone inserts were tested, the original design as shown in Figure 11 and a second one with a vane on the cone as shown in Figure 13. The last design was motivated to limit the amount of mercury left in the GLS when the mercury process loop is drained for maintenance. Since the mercury is radioactive, any mercury left in the GLS would lead to a higher dose in the hot cell and could lead to earlier sensor failures.

RESULTS

CFD results

Simulations of the first tested cone geometry showed adequate performance with a pressure drop of 37.7 kPa (equivalent to 8.6 factor loss) and a flow pattern that allowed helium to accumulate at the top of the GLS. These results aligned with early prototype experiments in water, so the cone design was not adjusted for greater or lesser pressure

loss. A comparison of the gas flow pattern between the cone design and no cone is shown in Figure 14. With no cone, the stratified gas layer begins to accumulate at the top of the GLS. Unfortunately, a steady vortex forms at the inlet of the next piping section, which entrains some of this gas pocket. By comparison, the cone allows the gas layer to build without disruption. The cone does not disturb the flow initially, allowing the stratified gas layer to rise through buoyant forces. The mercury, meanwhile, swirls around the cone before proceeding through the bottom gap to continue through the remaining piping. Based on the improved flow dynamics with only 26.6 kPa more pressure drop than a no cone design, we expected the base cone design to work well when tested for efficiency. The gas removal in the simulation was 100% (within numerical uncertainty), but the model was sufficiently simplified that this performance was unlikely during experiments.

The next set of experiments were run over six alternate cone designs that removed the bottom space of the GLS where mercury could accumulate, with various vanes to help improve the flow. To raise the cone and keep some level of efficiency, the inlet areas had to be reduced, increasing pressure drop. Iterative design lowered the pressure drop for the new cone from an initial 63.5 kPa to 39.7 kPa, or only 5.3% more compared to the initial design. This was achieved by strategically enlarging the cone inlet areas. The streamlines and helium iso-surfaces of this vaned design are shown in Figure 15 to highlight the low-speed mercury flow at the top of the GLS and the gas flow's qualitatively similar behavior.

The final design showed that a vane extending the left-side of the inlet to the cone helped to eliminate high shear forces that would disrupt the stratified gas layer as it

entered the new GLS design. These shear forces are higher in the new design, as there is no room for the swirling mercury flow to go under the incoming flow with the floor being raised to the inlet height, so the recirculating flow travels over the outlet pipe before shearing the incoming flow. Additionally, the new design included a spiral vane along the cone from the inlet to the top of the outlet pipe. Simulations showed this vane helped reduce the volume of mercury that was entrained under the cone when the flow first enters the GLS, which pulled some of the gas with it.

Finally, a single-phase, transient Reynolds stress model simulation was run for both geometries to ensure that the isotropic turbulence condition of the realizable k-ε was not under-resolving the turbulence in the GLS due to the rotational motion of the flow. Area-weighted averages of the turbulent kinetic energy were taken at various planes which showed that the k-ε model was under-resolving the turbulence by an average of 22.6% by not resolving the impacts of the swirling flow. Unfortunately, the Reynolds-stress model could not be run with the two-phase flow model due to high numerical instabilities, so the full impact of the higher turbulent forces on the gas flow could not be estimated. This vaned design still showed higher shear forces than the original cone design, but the simulations showed potential for over 90% gas removal while eliminating the concern with mercury accumulation in the bottom of the GLS.

Experimental results

The GLS was tested for a mercury flow range of 230 to 250 GPM and a gas injection rate of 2.5 to 20 SLPM. As predicted by Baker's map [7], the flow was found to be stratified at the inlet of the GLS for all tested flow regimes. The pressure loss factor for the GLS with

the simple cone and the vaned-cone was found to be, respectively, 8.3 and 11.1. The GLS efficiency is shown in Figure 16: the simple cone was found to have much better performance than the vaned one. For the simple cone, large gas bubbles were observed on the top of the GLS swirling towards the ventline. At a nominal flow rate of 250 GPM, its efficiency is above 90% for all the gas injection rates. At a lower mercury flow rate, higher efficiencies are observed at a gas injection rates below 15 SLPM. This can be explained by lower turbulence, which breaks the stratified gas layer into larger bubbles that rise more quickly to the top of the GLS due to larger buoyant forces. The lower efficiencies at a higher mercury flow rate can be explained conversely. At higher gas injection rates (>15 SLPM), larger gas pockets are formed at the top of the GLS, and no correlation with mercury flow rate can be found. Although the vaned-cone CFD results were promising, the efficiency was found poor at low gas injection rates (see Figure 16). One possible explanation is higher shear flow at the inlet compared to the simple cone, which generates smaller bubbles that are more easily entrained in the main mercury flow. Since the base of the cone is higher than the original cone, it is also easier for bubbles to be sucked at its base. As a baseline, measurements without any cone was also performed (see Figure 16): although it provide good performance at low gas injection rate, its efficiency decreases as gas injection rate increases.

DISCUSSION [All]

The design with the simple cone satisfies all SNS requirements. The efficiency is larger than 90% in the desired flow regime with a pressure low factor well below 20. The CFD

simulations were leveraged to explore the GLS design and it was found that the pressure drops was well-predicted and mainly dependent on the gap between the bottom of the enclosure and the bottom of the cone. Simulations showed a 3.6% error in the pressure loss prediction for the original cone design and a 18% loss for the spiral cone. The larger error in the spiral cone is believed to come primarily from manufacturing differences in the cone vanes. However, CFD simulations did not show great promise in identifying the separation performance of GLS designs. This is attributed to difficulties in modeling the change from the stratified entrance flow to the bubbly flow within the GLS. Greater accuracy in resolving the two phases and the turbulent state is likely required to increase this accuracy.

An additional vent at the top of the cone was also considered to remove any gas that would accumulate in the cone. However, this design complicated the geometry for remote operation which is not desired for SNS configuration. In addition, pressure drop can be tuned to desired values by modifying static or dynamic characteristics of the design by altering parameters such as wetted surface roughness, flow passages equivalent cross-sectional area, inner cone material permeation, vortex orientation, recirculation zones optimization, or addition of controlled external forces such as magnetic fields.

However, a conscious balance for a pressure distribution needs to be imposed to accumulate and evacuate the separated gas phase in a simple manner. A positive pressure gradient at the ventline is needed to provide optimal gas evacuation and avoid reverse gas filtration in the system. This condition ensures the unidirectional flow of gas from the inside of the GLS towards the conditions imposed at the outside of the gas evacuation line

(atmospheric in this case). The inner body of the shallow cone could be optimized to provide either an increased overall system pressure or an increased outlet liquid flow rate and therefore pressure drop. In addition, a second complementary phase separation chamber may be implemented.

CONCLUSION

A novel passive gas liquid-separator has been designed and tested. The design is such that it can replace a standard 90-deg horizontal elbow and thus, can be implemented in existing facilities without significant modifications and minimal impact. The design is based on the generation of an internal controlled vortex flow path with an internal flow deflector and a gas purging line. CFD simulations were used to explore several designs. Experiments were carried out in a mercury loop process injecting helium gas to measure the device performance. The results showed phase separation efficiency as high as 98% with minimal pressure drop. Two cone inserts geometries were tested under similar conditions and performance results were presented. The initial design —without vane deflectors— showed higher efficiencies in the range of 80 to 98% gas removal with respect to the vaned cone, which showed efficiencies in the 20% for low gas injection rates and up to 80% for higher flow rates. The difference in performance was attributed to an increase in turbulence mixing and increased interphase shear stress in the vaned design causing a redistribution of the gas flow regime.

ACKNOWLEDGMENT

REFERENCES

[1] C. Barbier, "Improving Computational Fluid Dynamics Simulations for the Spallation Neutron Source Jet-Flow Target," in *ASME 2016 Fluids Engineering Division Summer Meeting collocated with the ASME 2016 Heat Transfer Summer Conference and the ASME 2016 14th International Conference on Nanochannels, Microchannels, and Minichannels*, Washington DC, USA, 2016.

[2] D. A. McClintock, B. W. Riemer, P. D. Ferguson, A. J. Carroll and M. J. Dayton, "Initial observations of cavitation-induced erosion of liquid metal spallation target vessels at the Spallation Neutron Source," *J. Nucl. Mater.,* vol. 431, pp. 147-159, 2012.

[3] B. W. Riemer, M. W. Wendel, D. K. Felde, A. A. Abdou and D. A. McClintock, "Status of R&D on mitigating the effects of pressure waves for the Spallation Neutron Source mercury target," *Journal of Nuclear Materials,* vol. 431, no. 1, pp. 160-171, 2012.

[4] P. Rosenblad, M. Wendel, L. Jacobs, B. Riemer, D. Winder, C. Barbier, M. Dayton, G. Stephens, R. DeCosta, S. Parson and D. Freeman, "Initial implementation of helium Gas into the SNS mercury target for mitigation of fatigue and cavitation damage," *Journal of Physics: Conference Series,* vol. 1021, no. 1, p. 012073, 2018.

[5] Y. Liu, W. Blokland, C. Long, S. Murray, B. Riemer, R. Sangrey, M. Wendel and D. Winder, "Strain measurement in the recent SNS mercury target with gas injection," *In Journal of Physics: Conference Series,* vol. 1067, no. 5, p. 052022, 2018.

[6] M. Stewart and K. Arnold, Gas-liquid and Liquid-liquid Separators, Gulf Professional Publishing, 2008.

[7] O. Baker, "Speed-up flow calculations for design of gas gathering systems," *Oil and Gas Journal,* vol. 53, no. 12, pp. 185-190, 1954.

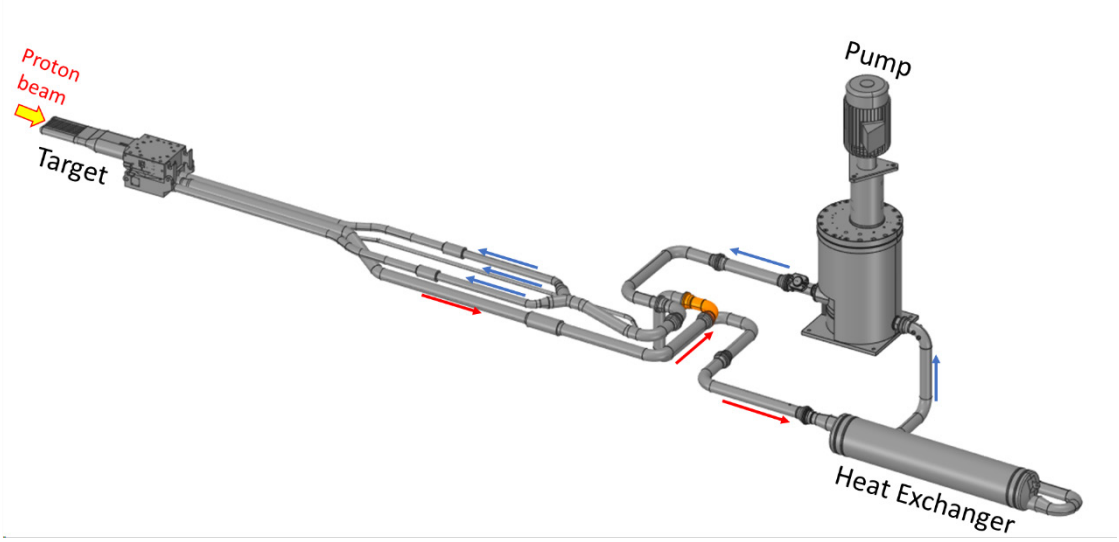

Figure 1. Schematic of the SNS mercury process loop; the arrows indicate the mercury flow direction as well as the hot and cold legs. The GLS will be installed in the 90-deg horizontal elbow shown in orange downstream of the target and upstream of the heat exchanger. For clarity, only major components are shown.

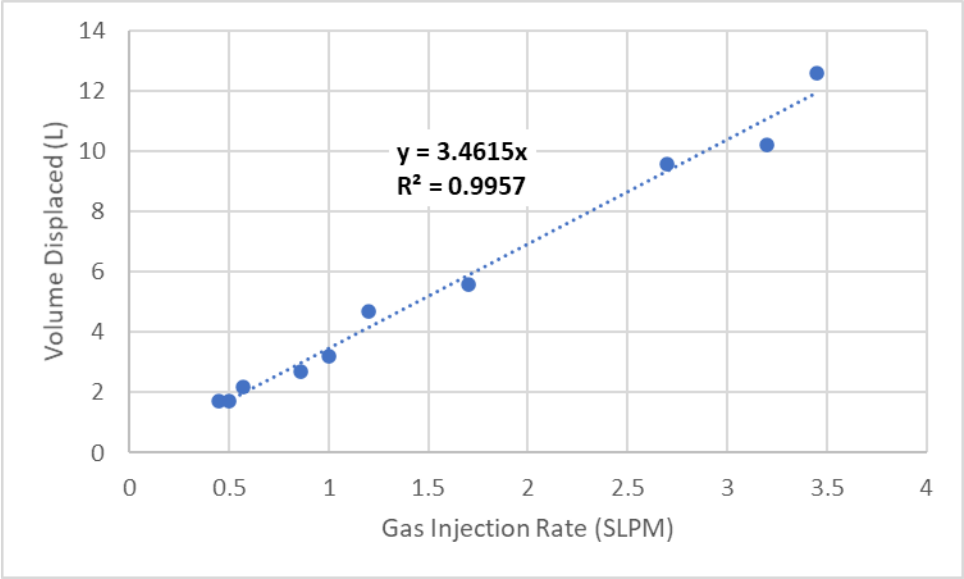

Figure 2. Gas accumulation in the process loop as a function of gas injection rate in the target.

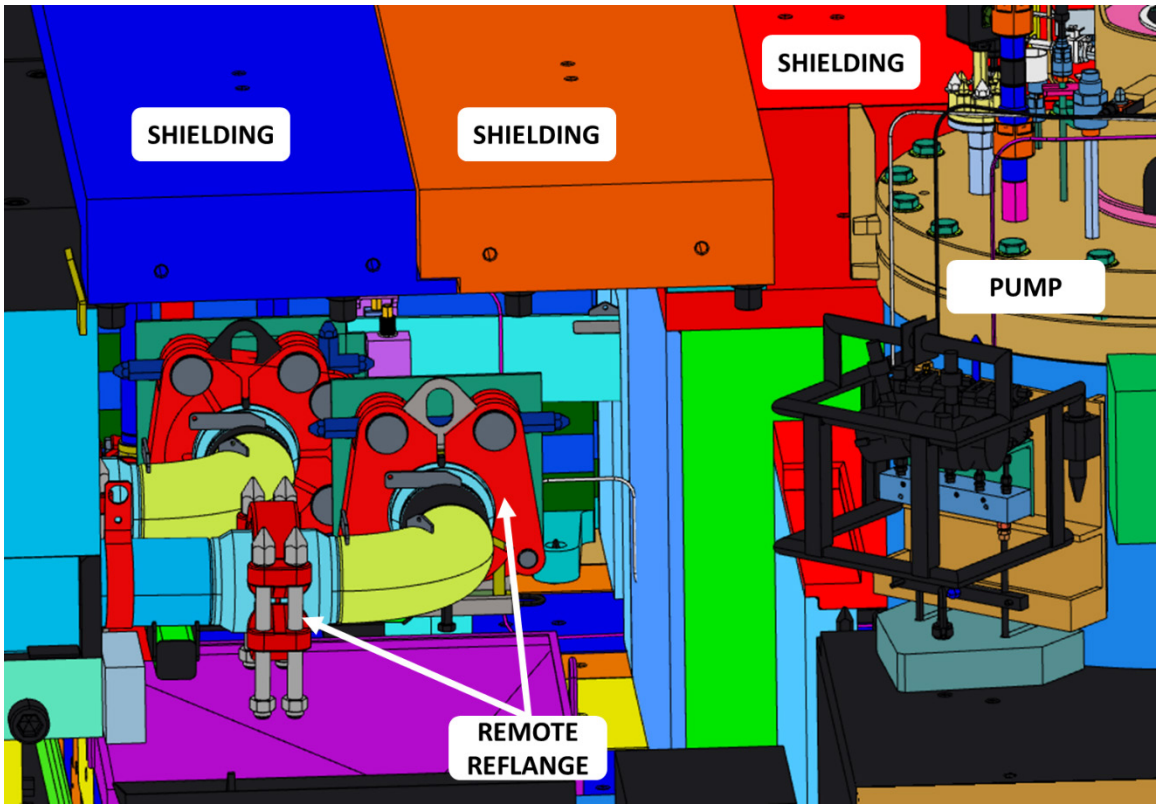

Figure 3. Geometrical constraints for the GLS due to the presence of shielding.

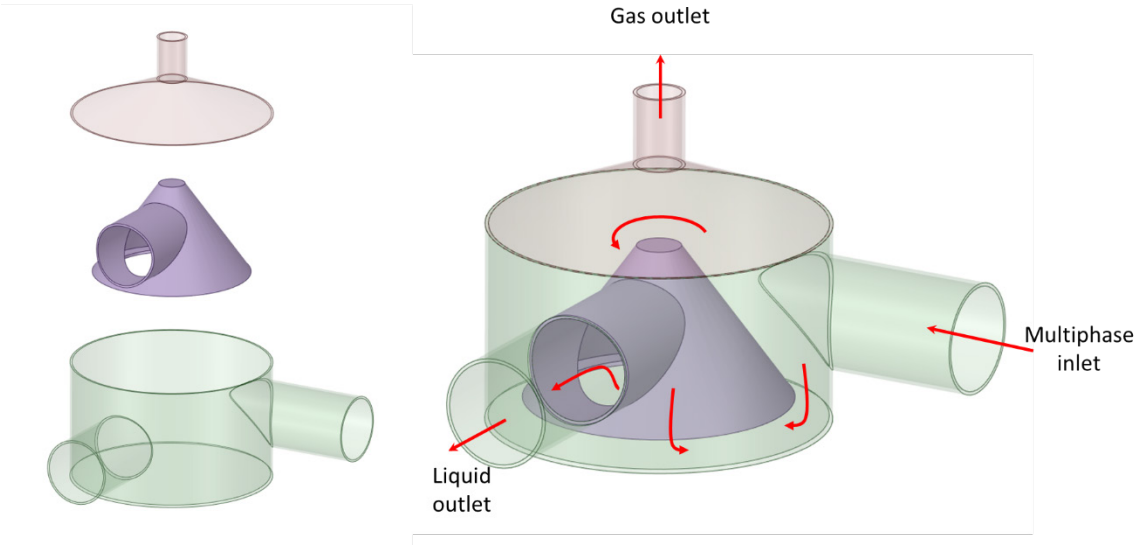

Figure 4. Concept of the compact GLS.

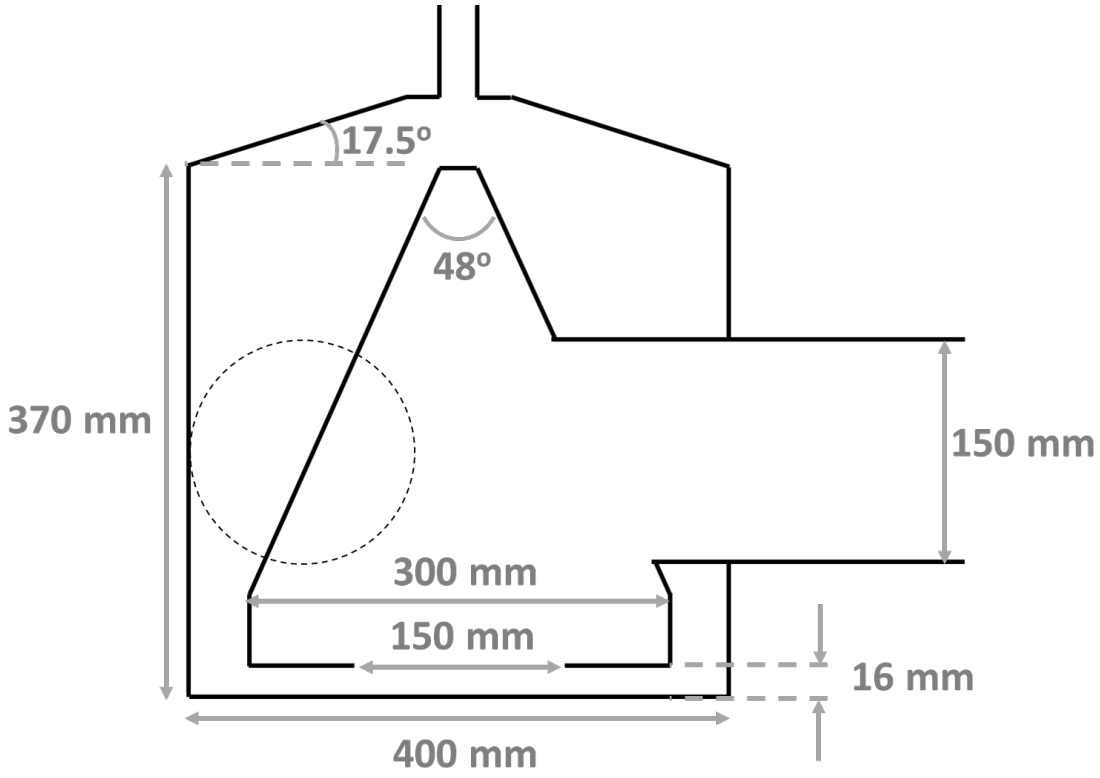

Figure 5. Typical dimensions used for the CFD analysis shown at the outlet midplane.

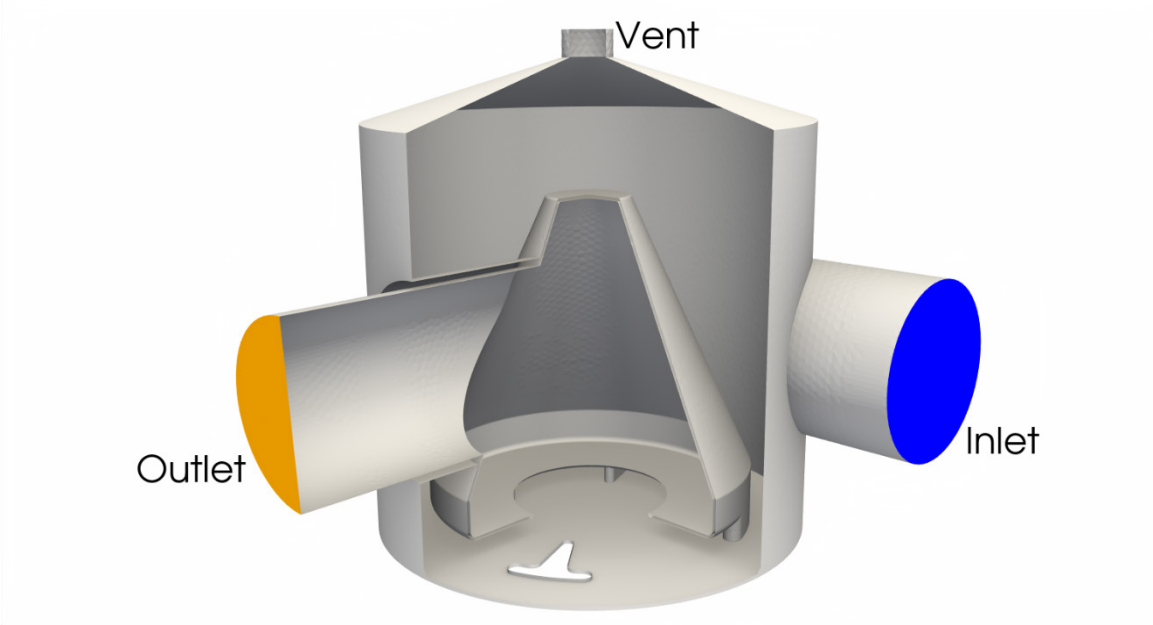

Figure 6. Geometry of nominal GLS design with boundaries highlighted

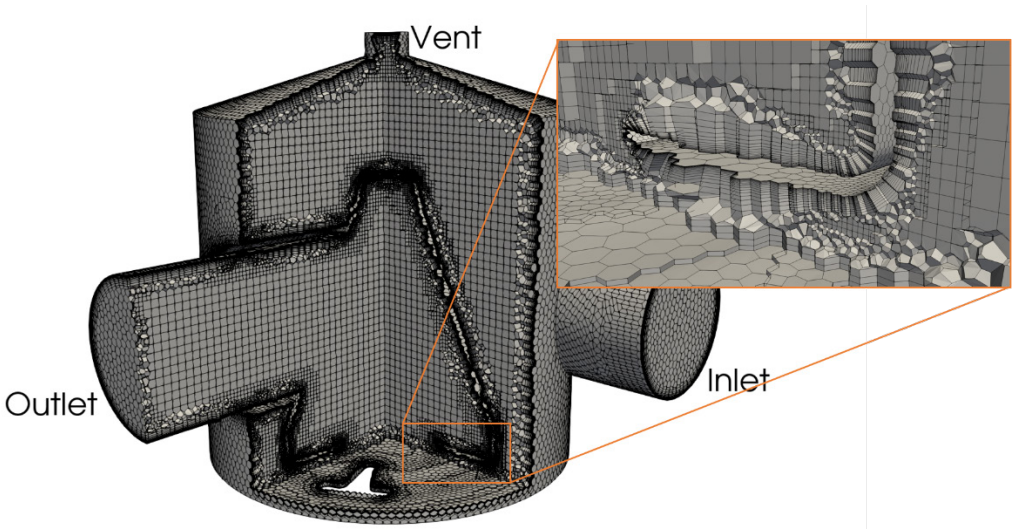

Figure 7. Cross-section view of mesh at the cone's center and aligned with the outlet. Detailed view shows mesh refinement near boundaries.

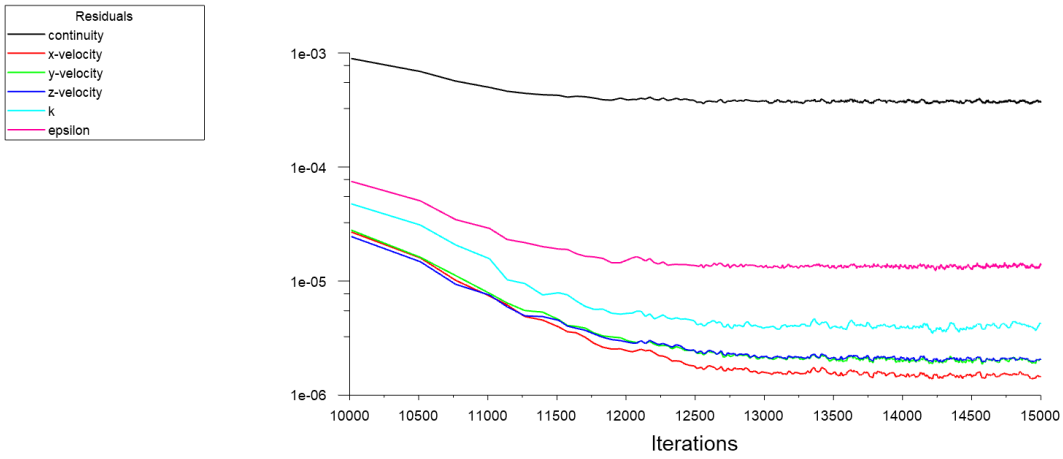

Figure 8: Residuals for single phase simulations. The simulation was restarted from an existing momentum solution at 10,000 iterations to speed convergence.

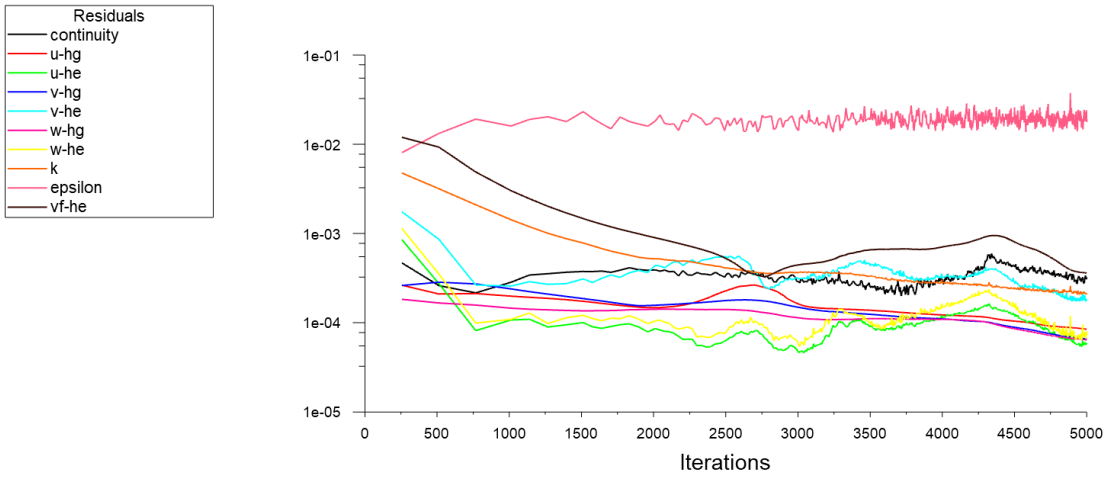

Figure 9: Residuals for two-phase simulations showing poor convergence of the turbulent dissipation rate and lack of steady behavior in conservation laws

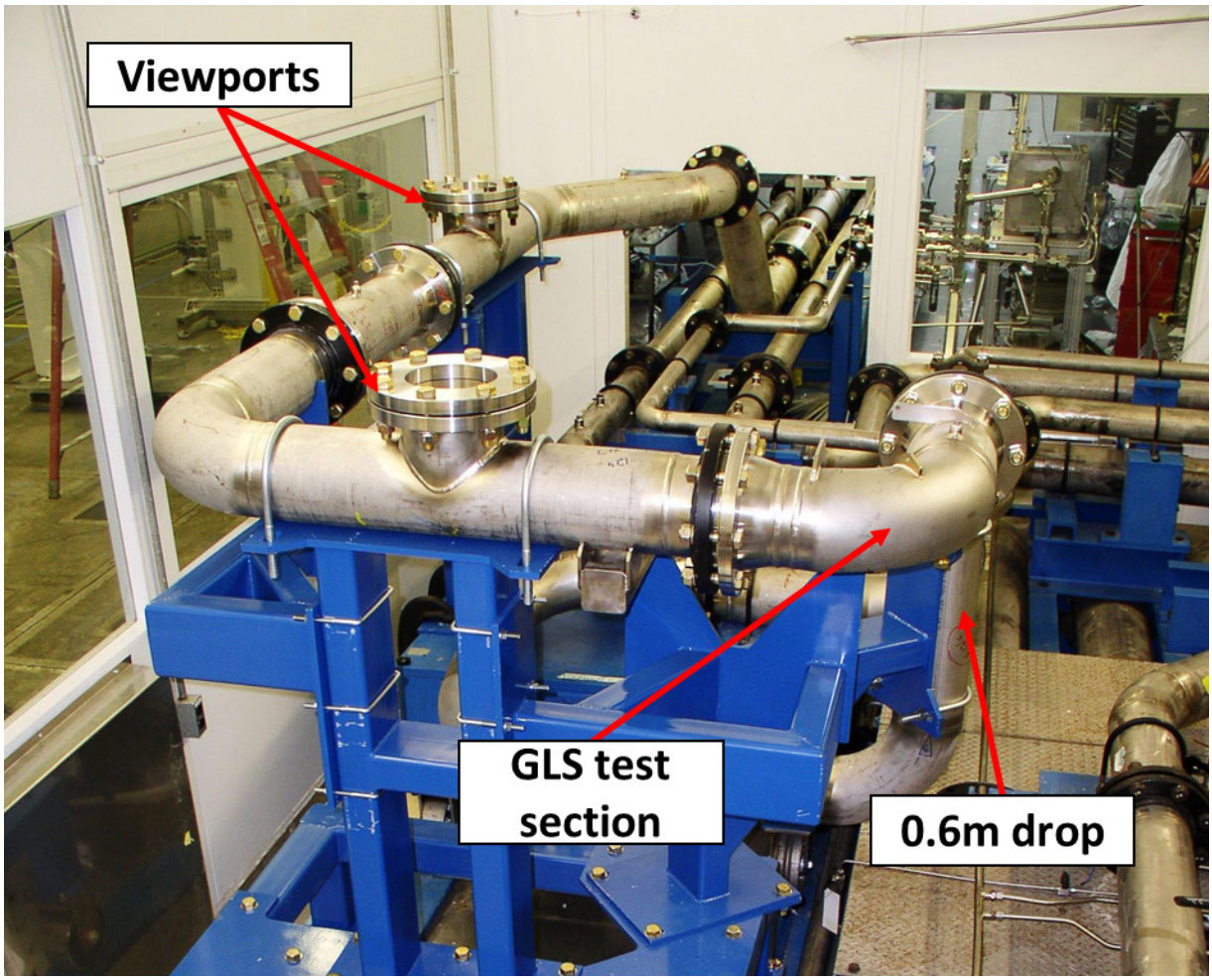

Figure 10. Picture of the GLS test section at the TTF.

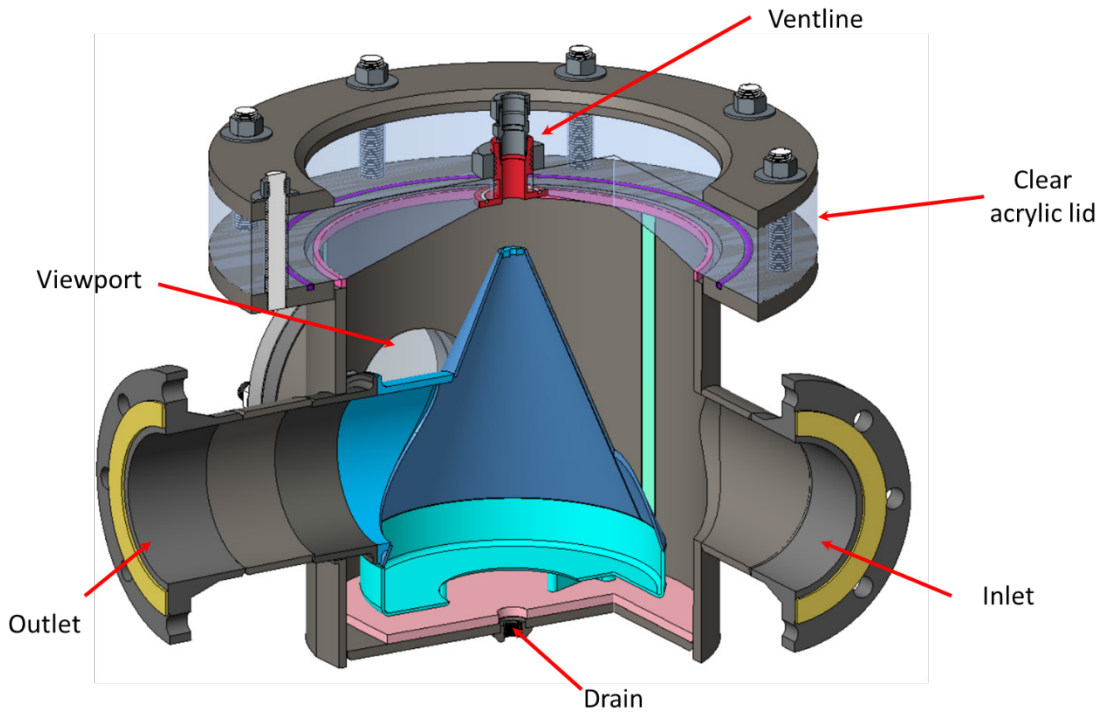

Figure 11. Cross-section view of the prototypical GLS.

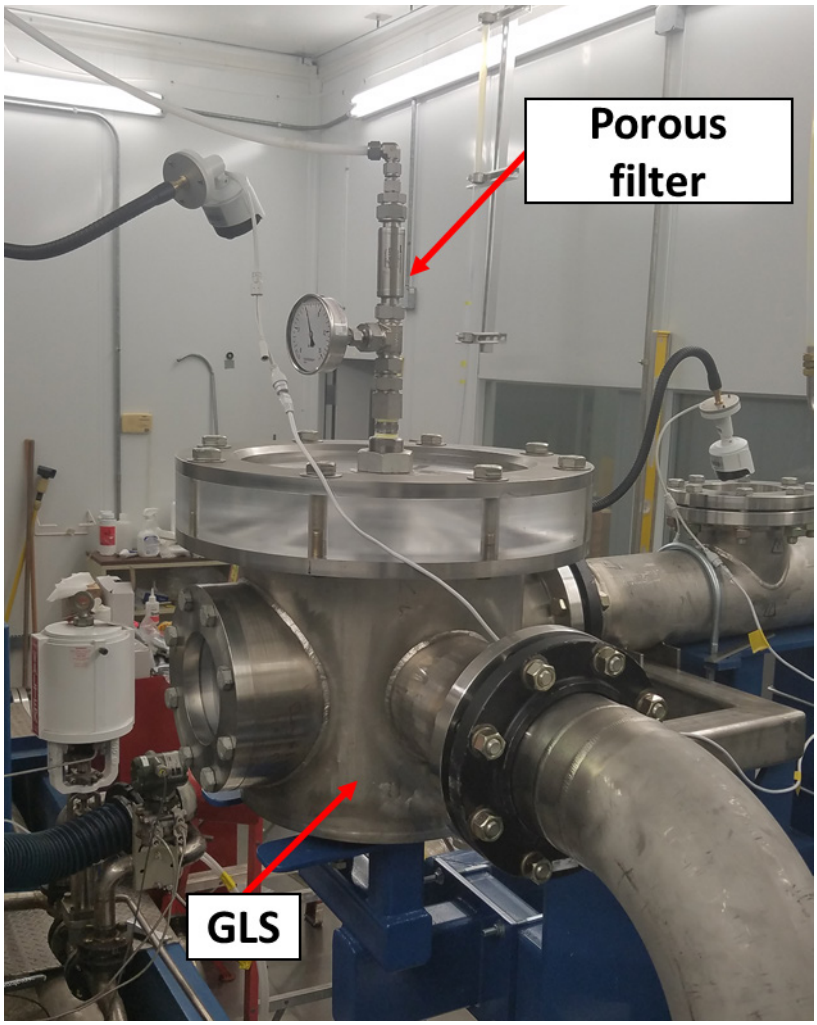

Figure 12. Picture of the GLS installed in the TTF loop and location of the porous filter on the GLS ventline.

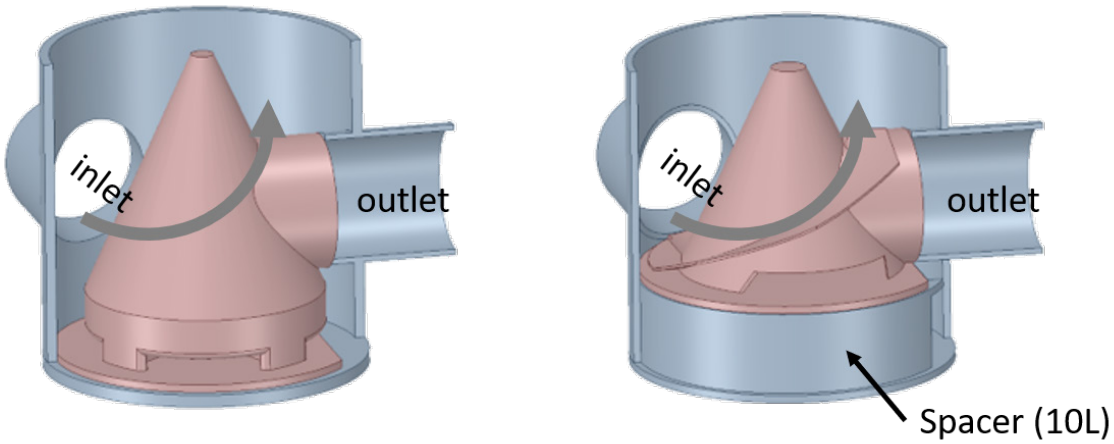

Figure 13. Illustration of the two cone inserts tested: the original (left) and the vaned cone (right).

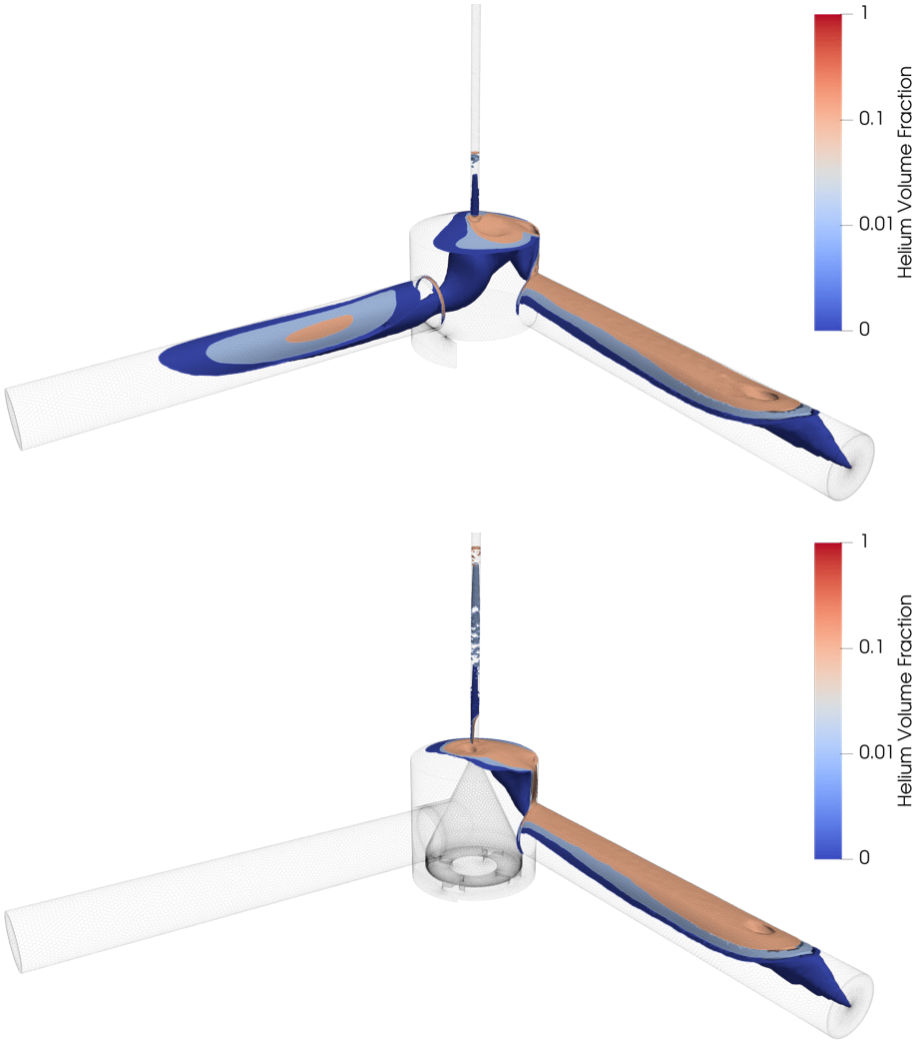

Figure 14: Comparison of two-phase flow within an empty GLS housing (top) and the first cone design (bottom) colored by helium iso-surfaces

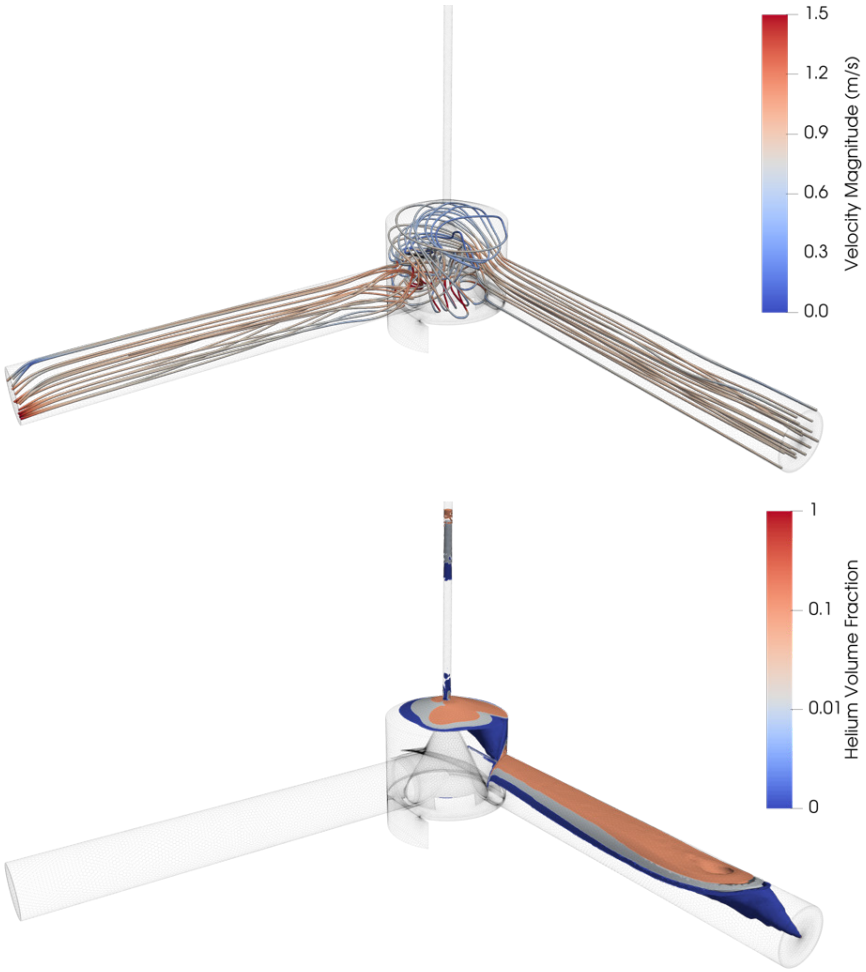

Figure 15: Streamlines colored by velocity(top) and helium iso-surfaces (bottom) of the vaned cone design

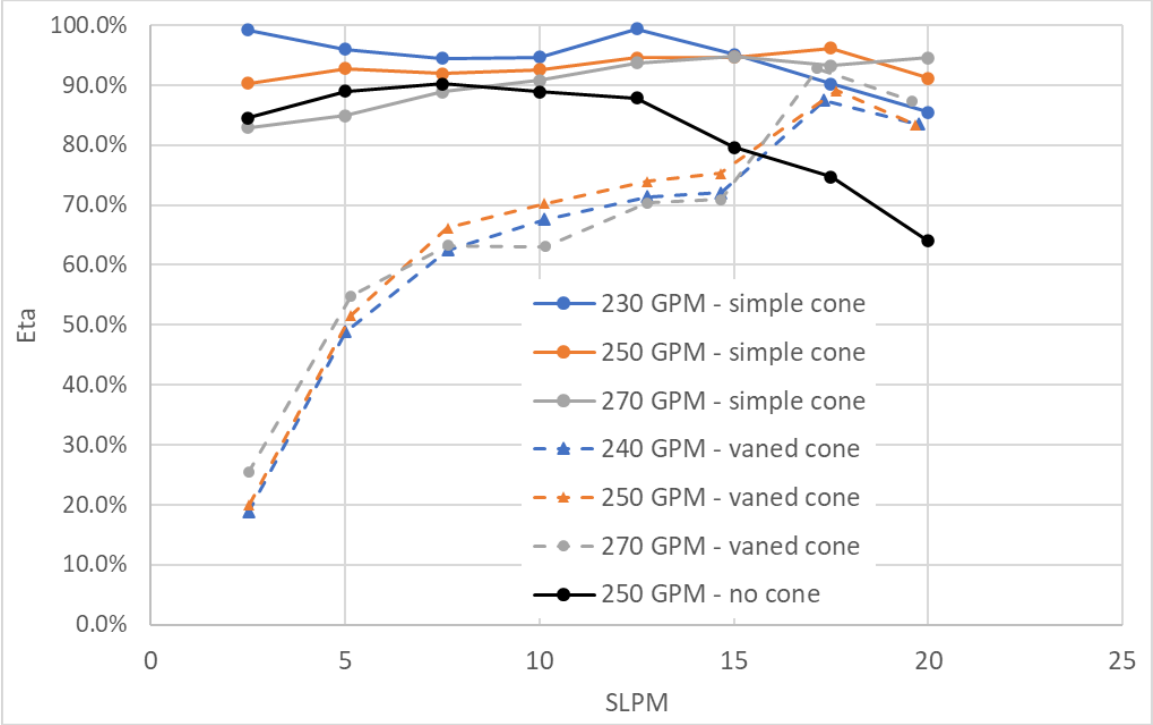

Figure 16. GLS efficiency for the two cone inserts for 3 mercury flow rates (from 230 to 270 GPM) and Helium flow rates (from 2.5 to 20 SLPM).

Table 1. Mesh dependence study results for simulations

Base Cell Size (mm)	Number of Cells	Average First Cell Y+	Vent Pressure	Cone Inlet Pressure
16	759,327	79.5	185,663	151,220
8	2,189,875	45.9	186,042	151,981
4	8,841,843	20.7	186,815	151,330